Chinese Chemical Letters 37 (2026) 110666

Contents lists available at ScienceDirect

Chinese Chemical Letters

journal homepage: www.elsevier.com/locate/cclet

A high-performance chemically self-charging aqueous zinc battery using a porous organic polymer cathode

Xiaojuan Chen[a], Yanwei Ma[b], Yiwen Lu[b], Huimin Zhang[b], Baozhu Yang[b], Qi Liu[a,b,*]

[a] School of Materials Science and Engineering and Jiangsu Key Laboratory of Advanced Catalytic Materials Technology, Changzhou University, Changzhou 213164, China

[b] Jiangsu Key Laboratory of Advanced Catalytic Materials and Technology, Advanced Catalysis Green Manufacturing Collaborative Innovation Center and School of Petrochemical Engineering, Changzhou University, Changzhou 213164, China

ARTICLE INFO

Article history:
Received 30 September 2024
Revised 7 November 2024
Accepted 21 November 2024
Available online 23 November 2024

Keywords:
Aqueous zinc batteries
Porous organic polymer
Organic cathode materials
Flexible air-rechargeable Zn-organic batteries
Self-powered system

ABSTRACT

In order to cope with harsh situations without an external power supply, developing high-performance aqueous zinc batteries (AZBs) with chemically self-charging as a self-powered system is of great practical significance. Herein, we present the synthesis of a new porous organic polymer with hexaazatriphenylene hexacarboxylic acid trianhydride (HHAT) and 2,6-diaminoanthraquinone (DAAQ) units (HTAQ). Due to its π-conjugated aromatic structure with abundant redox-active centers and limited solubility in electrolytes, the constructed flexible and coin-type AZBs based on HTAQ cathodes display a superior volume energy density (8.7 mWh/cm^3) and a higher energy density (104 Wh/kg), respectively, and excellent cycle life, where both Zn^{2+} and H^+ ions participate in the cathode reaction. Impressively, the electric energy exhausted flexible Zn//HTAQ AZB can be chemically self-recharged by exposing the discharged HTAQ cathode to air, ascribing to the spontaneous redox reaction between O_2 and the discharged HTAQ cathode. The exhausted flexible Zn//HTAQ AZB after air-charging for 30 h, can present a high discharge capacity of 294 mAh/g at 0.5 A/g, a higher self-charging cycle stability (15 cycles), a high-rate capability, and work well at hybrid modes (chemical or/and galvanostatic charging). Our work opens a new route to construct high-performance self-powered systems based on AZBs.

© 2025 Published by Elsevier B.V. on behalf of Chinese Chemical Society and Institute of Materia Medica, Chinese Academy of Medical Sciences.

In order to cope with increasing energy and environmental concerns, there is an urgent need to develop various high-performance storage energy systems [1,2]. Among them, rechargeable aqueous zinc batteries (AZBs) with high safety, low cost and environmental benignity have promising potential for application in large-scale energy storage stations, and wearable electronic products [3–7]. Usually, rechargeable batteries are typically charged using an external power source, however, the recharging and reuse of batteries may be restricted in remote or harsh environments where access to a power grid is limited [1,8]. This situation may be encountered when using wearable electronic products outdoors. To address this limitation, a promising approach involves the integration of rechargeable batteries with diverse energy harvesting systems, such as thermoelectrics [9], piezoelectric nanogenerators [10,11], photovoltaic devices [12,13], and triboelectric nanogenerators [14,15], thereby creating a self-powered system. Unfortunately, the aforementioned integrated systems are heavily reliant on energy resources that are not readily accessible at all times and in all locations, rely on usage scenarios, or have complex structures. Obviously, it is a significant work that constructing a self-powered system with a simple structure for wearable electronic products. Notably, unlike other environmental energy sources, air is ubiquitous, O_2 in air maintains a nearly constant concentration, and the chemical energy of oxygen can be turned into electrical energy through redox reactions, making it a readily available "energy resource" for various energy devices [16,17]. Therefore, harnessing the chemical energy of atmospheric O_2 in conjunction with rechargeable AZBs should be an effective approach for constructing self-powered systems with simple structures. Recently, some chemically self-charging AZBs *via* air oxidation (also called air-charging AZBs) have been reported, but the research in this area is still in its early stages [17–25]. For instance, an AZB with air-charging capability was reported by Niu et al. in 2020, wherein the spontaneous redox reaction can happen between the discharged inorganic cathode ($CaZn_{3.6}VO$) and oxygen in air along with the removal of Zn^{2+} ions [18]. Recently, Niu *et al.* and Liu *et al.* respectively constructed chemically self-charging AZBs based on organic cathode materials BQPH and TNHATN, wherein the process

* Corresponding author.
E-mail address: liuqi@cczu.edu.cn (Q. Liu).

https://doi.org/10.1016/j.cclet.2024.110666
1001-8417/© 2025 Published by Elsevier B.V. on behalf of Chinese Chemical Society and Institute of Materia Medica, Chinese Academy of Medical Sciences.

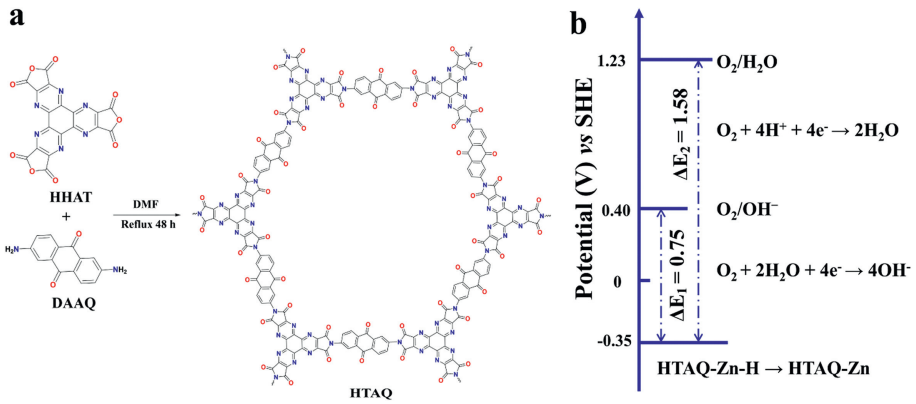


Fig. 1. (a) Synthetic diagram of HTAQ. (b) Energy level transition diagram for the discharged HTAQ cathode (HTAQ-Zn-H) and O_2.

of redox reaction between the discharged BQPH/TNHATN and O_2 involves the removal of H^+ ions [22,23]. However, the above-mentioned AZBs present limited air-charging cycle stability (only four to six cycles) or limited discharge capacity after air oxidation [18,22,23]. Obviously, the next challenge is to construct AZBs with both high discharge capacity and air-charging cycling stability. Owing to the potential difference between oxygen and discharged cathode being the main factor determining the chemically self-charging ability of AZBs, the choice of cathode material is crucial.

Porous organic polymers (POPs) are an emerging class of organic polymers constructed by covalent bonds and organic units, which present several characteristics of conjugated skeleton, inherent porosity and uniform pore sizes, and controllable crystalline or amorphous state [26–29]. These characteristics result in their insolubility in aqueous solutions and organic solvents, as well as high electronic/ionic conductivity [30–32]. Moreover, by introducing redox-active groups into the skeleton structure of POPs, the application of POPs can extend to the energy storage field [33–36]. On the other hand, many studies have demonstrated that π-conjugated aromatic compounds including redox groups (carbonyl/imine, C=O/C=N) can act as high-performance cathode materials for AZBs, owing to the C=O/C=N groups can interact with Zn^{2+}/H^+ ions [37–54]. To realize the goal of constructing AZBs with both high discharge capacity and air-charging cycling stability, building large conjugate systems *via* introducing redox-active groups into the backbones of POPs should be a feasible and effective strategy. Based on this idea, herein, we synthesized a new porous organic polymer including hexaazatriphenylene hexacarboxylic acid trianhydride (HHAT) and 2,6-diaminoanthraquinone (DAAQ) units (HTAQ), owning π-conjugated aromatic structure and multiple redox-active centers (C=O and C=N) (Fig. 1a), and built coin-type and flexible chemically self-charging capability AZBs based on HTAQ cathode. As expected, the assembled coin-type and flexible Zn//HTAQ AZBs not only display better rate performance and excellent cycle life, but also remarkable energy density (104 Wh/kg) and superior volumetric energy density (8.7 mWh/cm^3), respectively. Impressively, the electric energy exhausted flexible Zn//HTAQ AZB can be chemically self-recharged by exposing the discharged HTAQ cathode (HTAQ-Zn-H) to air for varying durations, ascribing to the spontaneous redox reaction between O_2 and HTAQ-Zn-H (Fig. 1b). The exhausted flexible Zn//HTAQ AZB after air-charging for 30 h, can present a high discharge capacity (294 mAh/g at 0.5 A/g), a higher self-charging cycle stability (15 cycles) and a high-rate capability (105 mAh/g at 20 A/g). This work reveals that the performance improvement of air-charging AZBs can be realized *via* the rational design of POPs with extended conjugated structures and multi-redox active groups.

HTAQ with dual redox active sites (C=O and C=N) was synthesized by using the condensation reaction between HHAT and DAAQ (Fig. 1a). The successful synthesis of HTAQ was demonstrated by solid-state ^{13}C nuclear magnetic resonance (^{13}C SSNMR) spectroscopy, Fourier-transform infrared spectroscopy (FT-IR), and powder X-ray diffraction (XRD) pattern. All peaks in the ^{13}C SSNMR of HTAQ are marked in the indicated groups of the inset chemical structure (Fig. S1 in Supporting information). The FT-IR spectrum of as-synthesized HTAQ exhibits two distinct absorption peaks at 1629 and 1571 cm^{-1} (Fig. S2 in Supporting information), which can be assigned to the stretching vibration modes of carbonyls/imines (C=O/C=N) and the stretching vibration of the benzene ring, respectively. The XRD patterns reveal precursor DAAQ has high crystallinity, and HTAQ material owns amorphous characteristics (Fig. S3 in Supporting information). Thermogravimetric analysis shows that HTAQ material has good thermal stability before 320 °C (Fig. S4 in Supporting information). The FESEM image of HTAQ material in Fig. S5 (Supporting information) shows it is composed of nanoparticles with size of 40–70 nm. Raman spectrum of HTAQ is shown in Fig. S6 (Supporting information). The peak at 1524 cm^{-1} in the Raman spectrum belongs to the D band, which derives from C (sp^3) and curved C (sp^2). The peak at 1635 cm^{-1} belongs to the G band, which derives from sp^2 C with a conjugated structure. The I_D/I_G ratio is 0.48, indicating that there are certain defects in the structure of HTAQ, which is conducive to ion transport [33]. The specific surface area, the pore volume, and the pore size distribution of HTAQ material were measured *via* N_2 adsorption-desorption technique. As indicated in Fig. S7 (Supporting information), according to the type of the adsorption-desorption isotherms, most of the void space in HTAQ material stems from mesoporous, so, HTAQ is a mesoporous material. The pore volume and the specific surface area of HTAQ material are 0.050 cm^3/g and 11.84 m^2/g, respectively. Such low specific surface area might be ascribed to the disorder stacking of the POP layers [27,53]. Further, pore size distributions were calculated based on the Barret-Joyner-Halenda (BJH) method and an average pore size of 19.75 nm was determined. It is noteworthy that such a low surface area and mesoporous nature account for the chemical interaction of ions with the host POP material following the redox *pseudo*-capacitance mechanism rather than physical capacitance adsorption [47].

Using Zn//HTAQ coin-type batteries, the electrochemical properties of the HTAQ cathode were evaluated. Fig. 2a displays cyclic voltammetry (CV) curves of the HTAQ electrode cycled for four cycles at 0.5 mV/s in the range of 0.1–1.45 V. From Fig. 2a, it can be seen that there are a pair of obvious redox peaks and a pair of weaker redox peaks on each curve, indicating the existence of multi-step redox reactions during discharge-charge. The formation of the oxidation/reduction peaks should have belonged to the

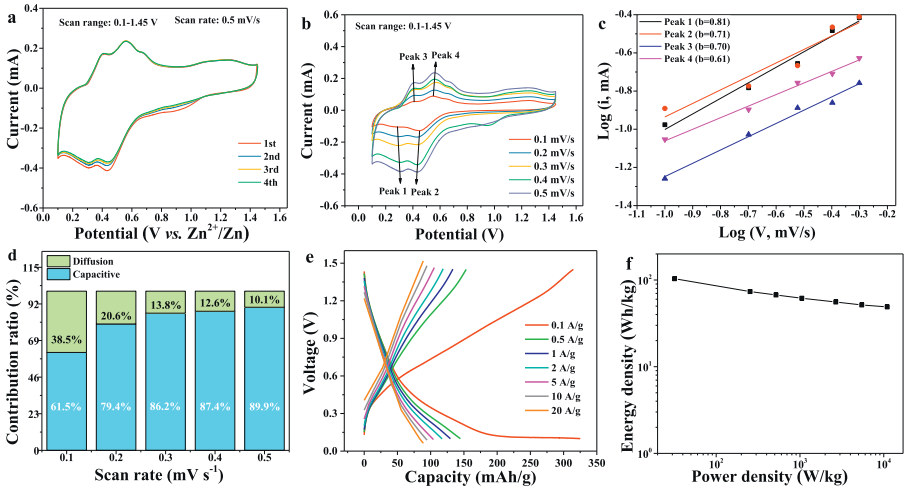


Fig. 2. (a) CV curves of HTAQ at 0.5 mV/s. (b) CV curves of the HTAQ electrode at different scan rates ranging from 0.1 mV/s to 0.5 mV/s. (c) Determination of the *b*-values. (d) The contribution ratios of the diffusion-controlled capacities and capacitive capacities at different scan rates. (e) GCD profiles at the current densities range from 0.1 A/g to 20 A/g. (f) Ragone plot of Zn//HTAQ battery.

removal/uptake of Zn^{2+}/H^{+} ions. The CV curves of three consecutive cycles from the second cycle beginning are not much different, indicating the HTAQ electrode has good reversibility. For studying the HTAQ electrode reaction kinetics, its CV curves at different scan rates of 0.1–0.5 mV/s were measured (Fig. 2b). Generally, the total capacity can be quantified as diffusion-controlled and capacitive processes. To evaluate the degree of capacitive effect, the power law ($i = a\nu^{b}$) is used, where i and ν stand for the peak current and the scan rate, respectively, and a and b are constants, $b = 1.0$ for a capacitive storage process and 0.5 for a diffusion-controlled process. The b value was calculated by the linear curve ($i = a\nu^{b}$) based on the CV curves [55]. It can be found in Fig. 2c that the b-values of the four peaks are 0.81, 0.71, 0.70, and 0.61, respectively, revealing the combined effect of capacitive and ionic diffusion behavior [17]. In addition, according to the equation $i = k_1\nu + k_2\nu^{1/2}$, the relative contributions of capacitive ($k_1\nu$) and diffusion-controlled ($k_2\nu^{1/2}$) processes can be calculated, where k_1 and k_2 are adjusted parameters at particular scan rates [56,57]. When the scan rate increases from 0.1 mV/s to 0.5 mV/s, the ratio of capacitive contribution also gradually increases from 61.5 % to 89.9 % (Fig. 2d and Fig. S8 in Supporting information), verifying the capacitive effect is gradually strengthening.

The Galvanostatic charge-discharge (GCD) curves of the HTAQ electrode at various current densities in the voltage range of 0.1–1.45 V are presented in Fig. 2e. As depicted in Fig. 2e, the HTAQ electrode can provide a high discharge specific capacity of 325 mAh/g at 0.1 A/g, which is lower than that of theoretical capacity for HTAQ (538 mAh/g, considering one HTAQ repeated unit obtaining 30 electrons). In order to deduct the capacity contribution of conductive carbon Ketjen Black, we prepared the Ketjen Black electrode and tested its charge-discharge curves at different current densities (Fig. S9 in Supporting information), the Ketjen Black electrode exhibited a capacity of 19 mAh/g at 0.1 A/g. Based on Eq. S1 (Supporting information) calculation, the discharge capacity of the HTAQ electrode after excluding Ketjen Black capacity contribution is 287 mAh/g at 0.1 A/g. The capacity of 287 mAh/g is also higher than that of many reported POPs and covalent organic frameworks (COFs) materials (Table S1 in Supporting information). When the current density increases to 0.5, 1, 2, 5, 10 and 20 A/g, the discharge capacities of 145, 130, 117, 104, 94 and 89 mAh/g can be kept, respectively, showing high-rate performance. Furthermore, the galvanostatic intermittent titration technique (GITT) was further employed to investigate such a fast reaction kinetics [17,21,22,54], where the Zn^{2+} ion diffusion coefficient is between 10^{-7}–10^{-8} cm^2/s (the detailed calculation process can be seen in the Supporting information), as shown in Figs. S10a and b (Supporting information), higher than that of other cathode materials reported [21,22,54]. Such fast transfer of Zn^{2+} ions endows the HTAQ electrode with high-rate performance. On the other hand, as shown in Fig. S10c (Supporting information), although the volume resistivity of the HTAQ organic compound is relatively high (1.5983×10^{10} Ω cm), the resistivity of the prepared HTAQ electrode (including HTAQ active material, Ketjen Black, and polyvinylidene fluoride) is reduced by three orders of magnitude (2.4228×10^{7} Ω cm), which is also beneficial for the migration of zinc ions. When the current density returns to 0.1, 0.5 and 1 A/g, the average discharge capacity still remains at 168, 126 and 115 mAh/g, respectively (Fig. S11a in Supporting information and Fig. 2e). After 2000 cycles at 2 A/g, the capacity retention is 72 %, and the Coulombic efficiency is close to 100 %, showing its excellent cycle stability (Fig. S11b in Supporting information).

For further investigating the stability of the electrode, dissolution experiments of the electrode were carried out. The HTAQ electrodes after 2000 cycles at 2 A/g were soaked in 2 mol/L $ZnSO_4$ electrolyte at different times (Fig. S12 in Supporting information), then, the changes in the electrolyte color were observed. We can find that the electrolyte is still clear after the electrode is soaked in the electrolyte for one month. Furthermore, from UV–vis curves of 2 mol/L $ZnSO_4$ electrolyte before and after the HTAQ electrode immersion (Fig. S13 in Supporting information), no absorption peak is observed. These facts indicate that HTAQ in the electrode is insoluble in the electrolyte. This insolubility should be attributed to HTAQ having a stable π-conjugated structure. The insoluble nature of HTAQ is favored to enhance the cycle stability of its electrode, which has been demonstrated by the cycling performance mentioned above. The Ragone plot of the Zn//HTAQ battery was calculated according to the calculation formula of energy density and power density (Note S1 in Supporting information, considering the mass of the HTAQ) and the discharged data presented in Fig. 2e, the results were depicted in Fig. 2f. It can be seen from Fig. 2f that the highest energy density can reach 104 Wh/kg at the power density of 31.9 W/kg, and highest power density has 11.0 kW/kg at the energy density of 48.9 Wh/kg. The output of this energy density (104 Wh/kg) is also good in the reported aqueous Zn battery (Table S2 in Supporting information) [42,50,58–64]. However, when the loading ratio of the active material HTAQ

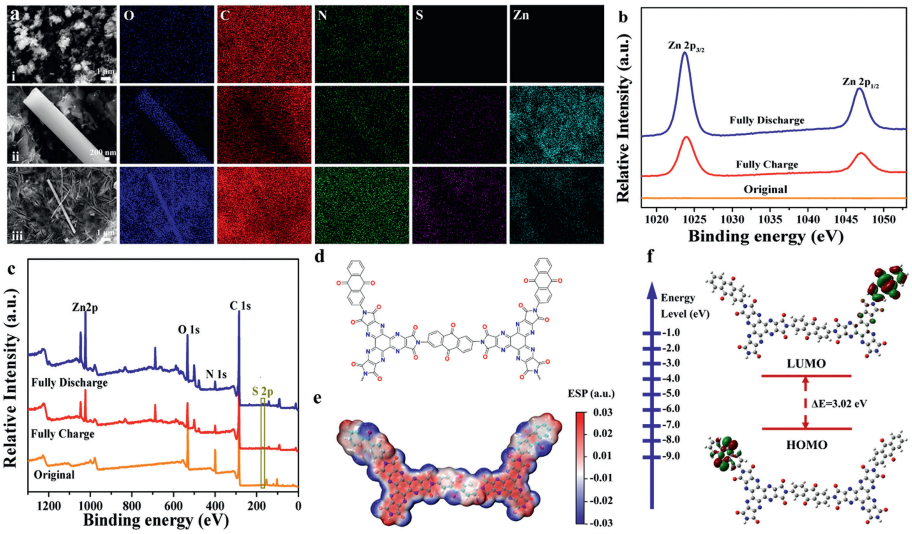


Fig. 3. (a) SEM images of the HTAQ electrodes (i) pristine, (ii) fully discharged (0.1 V) and (iii) fully charged (1.45 V) states and FESEM-EDS distribution mapping of O, C, N, S, Zn elements. (b) High-resolution XPS spectra of Zn 2p and (c) full XPS spectra of the HTAQ electrodes at pristine, fully discharged (0.1 V) and fully charged (1.45 V). (d) Repeated unit of HTAQ for DFT computation. (e) The ESP-mapped molecular van der Waals surface of the HTAQ repetitive unit; surface local minima of ESP are represented as blue spheres, and the corresponding ESP values are marked out by numbers. (f) Electronic structures of HOMO-LUMO orbital and relative energy level of HTAQ repeated unit obtained from DFT calculations.

increases, the discharge capacity significantly decreases (Fig. S14 in Supporting information), which is ascribed to organic materials having higher resistance. In spite of this, owing to the abundant sources of organic materials, the application of them in large-scale storage systems is promising.

To study the working mechanism of the HTAQ electrodes, a series of *ex-situ* physical methods are used to characterize the HTAQ electrodes in different states. By comparing the SEM-EDS images of the HTAQ cathode in the pristine, fully discharged and fully recharged state, we can observe that a large amount of Zn^{2+} ions appear in the discharged HTAQ electrode, and some Zn^{2+} ions still remain in the recharged electrode (Fig. 3a), revealing Zn^{2+} ions are inserted in the electrode during the discharge and some Zn^{2+} ions are removed from the electrode during the recharge. As displayed in Figs. 3b and c, *ex-situ* the XPS spectra of Zn 2p have also verified this change. Two distinct peaks, ascribed to Zn $2p_{3/2}$ and Zn $2p_{1/2}$, respectively, appear on the XPS spectrum of the HTAQ electrode after the first discharge from 1.45 V to 0.1 V, which illustrates the production of Zn^{2+} ions; the intensity of these two peaks weaken obviously after charging to 1.45 V, indicating that the Zn^{2+} ions have been partially removed. The reaction functional groups, namely the reaction centers, were determined by *ex-situ* infrared spectrum testing of the electrode materials under different charging and discharging states, and the working mechanism was further explained by the intensity change of the infrared characteristic peak under different degrees of charging and discharging (Fig. S15 in Supporting information). The peak located at 1629 cm^{-1} corresponds to the characteristic peaks of C=N/C=O (Figs. S15c and d). With the deepening of the discharge reaction, the intensity of the peak of C=N/C=O gradually weakens, indicating that Zn^{2+}/H^+ ions are coordinated with N/O atoms from C=N/C=O groups in the discharge process; when the electrode is charged from 0.4 V to 1.45 V, the peak intensity of C=N/C=O gradually recovers, indicating that this is the process of removing Zn^{2+}/H^+ ions from HTAQ (Fig. S15b). The above results indicate that the imine/carbonyl groups (C=N/C=O) are the redox-active centers of HTAQ, and there is an electrochemical reaction between it and Zn^{2+}/H^+ions. The intercalation mechanism of Zn^{2+} and H^+ ions was further verified by XRD patterns of the pristine electrode, the discharge electrode and the charge electrode (Fig. S16 in Supporting information). As shown in Fig. S16, new diffraction peaks at 7.92°, 14.92°, 21.27°, 27.58°, 27.76°, 28.52°, 32.69°, 37.21°, 41.23°, 58.36°, 59.22°, and 64.08° appear in the pattern of the discharge electrode, indicating the formation of $Zn_4(OH)_6SO_4{\cdot}5H_2O$ (PDF #39-0688). While most diffraction peaks from $Zn_4(OH)_6SO_4{\cdot}5H_2O$ disappear or the peaks intensities weaken in the charging state, indicating that a small part of $Zn_4(OH)_6SO_4{\cdot}5H_2O$ did not dissolve during the charging process. Furthermore, XPS spectra for S 2p (169.9 eV) presented in Fig. 3c also demonstrate the production of the hydroxide. The formation of $Zn_4(OH)_6SO_4{\cdot}5H_2O$ originates from the increase of OH^- ions concentration near the cathode caused by the coordination interaction between H^+ ions and HTAQ.

To further investigate the uptake/removal of Zn^{2+} and H^+ ions in the discharge-charge process, CV curves of the HTAQ electrode were tested in two electrolyte solutions (0.05 mmol/L H_2SO_4 of pH 4.14 and 2 mol/L $ZnSO_4$ of pH 4.14) using a three-electrode system, in which the HTAQ electrode was used as the working electrode, Ag/AgCl as the reference electrode, and platinum foil as the counter electrode. The scanning rate was set at 0.5 mV/s, and the results are presented in Fig. S17 (Supporting information). As shown in Fig. S17, the integral area of the CV curve in 2 mol/L $ZnSO_4$ is larger than that of the CV curve in H_2SO_4 electrolyte of pH 4.14, and integral areas of them partially overlap, which means Zn^{2+} and H^+ ions are all inserted into HTAQ. Besides, to eliminate the influence of H^+ ions on electrode performance, we measured the GCD curves of the HTAQ electrode in non-aqueous electrolyte (1 mol/L zinc trifluoromethane sulfonate (ZnTFS) in acetonitrile (ACN). As depicted in Fig. S18 (Supporting information), the capacity of the HTAQ electrode in 1 mol/L ZnTFS/ACN electrolyte can reach 119 mAh/g, but is lower than that of it in 2 mol/L $ZnSO_4/H_2O$ (145 mAh/g). The above facts further certify the co-uptake/co-removal of H^+ and Zn^{2+}ions in the discharge-charge process.

To further ascertain the exact electrochemical active sites for Zn^{2+}/H^+ anchoring in HTAQ, its repeated unit shown in Fig. 3d is analyzed using DFT calculation as a target molecule, and the electrostatic potential (ESP) mapping of the repeated unit for HTAQ can be obtained (Fig. 3e). Herein, the negative ESP (blue) reflects the affinity of the sites toward Zn^{2+}/H^+ ions uptake. According to the ESP mapping, the positions near N/O atoms from C=N/C=O groups

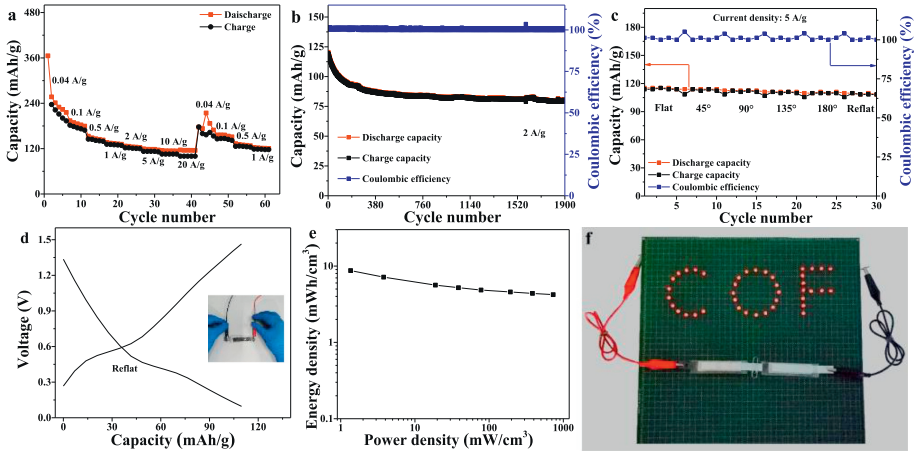


Fig. 4. Electrochemical properties of flexible Zn//HTAQ battery: (a) Rate performance. (b) Cycling performance at 2 A/g. (c) Cycle performance of flexible Zn//HTAQ battery bending from flat to reflat state at 5 A/g. (d) GCD curve of the flexible battery at the reflat state at 5 A/g. (e) Ragone plot of the flexible Zn//HTAQ. (f) Image of LED lights powered by flexible Zn//HTAQ batteries.

exhibit more negative ESP values, revealing that the active centers of HTAQ are the N/O atoms. Thus, within the channels of the HTAQ, C=N and C=O groups can efficiently coordinate with Zn^{2+}/H^+ ions *via* the N/O atoms. Besides, the energy levels of the HOMO and LUMO were presented in Fig. 3f. It can be found from Fig. 3f that HTAQ exhibits a lower LUMO energy level of −4.10 eV, revealing it has a better electron affinity in theory, this may be due to the occurrence of redox-active groups (C=N and C=O) in the material. In addition, HTAQ has a lower energy gap (E_g) of 3.02 eV due to its π-conjugated N-containing heteroaromatic structure. This lower E_g will be favored to enhance its electrochemical performance [49]. Fig. S19a (Supporting information) displays the optimized structure of the HTAQ repeated unit combined with 12 Zn^{2+} ions (HTAQ repeated unit-12 Zn). As can be seen from Fig. S19a, the Zn^{2+} ion coordinates with N and O atoms in the HTAQ unit, while the binding energy of HTAQ repeated unit-12 Zn is negative (Table S3 in Supporting information), implying C=N and C=O are active sites for Zn^{2+} coordination in HTAQ. Similarly, from the negative values of binding energies for HTAQ repeated unit-30H and HTAQ repeated unit-12Zn-6H (Table S3), we can infer H^+ions can also coordinate with N and O atoms in the HTAQ (Figs. S19b and c in Supporting information). Thus, the possible reaction mechanism for the HTAQ electrode described simply is as follows (the detailed process is shown in Fig. S20 in Supporting information):

$$\mathrm{HTAQ} \underset{+30e^-,\ +nZn^{2+},\ +(30\text{-}2n)H^+}{\overset{+30e^-,\ +nZn^{2+},\ +(30\text{-}2n)H^+}{\rightleftharpoons}} \mathrm{HTAQ\text{-}nZn\text{-}(30\text{-}2n)H} \quad (1)$$

It can be found in Fig. S20 that the HTAQ unit is reduced to the $HTAQ^{30-}$ unit after it obtains 30 electrons from the losing electrons of the Zn anode, subsequently, HTAQ-nZn-(30–2n)H is produced *via* the combining of H^+ and Zn^{2+} ions with N/O atoms in the $HTAQ^{30-}$ unit. The opposite process happens during charging. Similar reaction mechanisms have also been proposed for other organic cathodes [47,49].

In order to study the application prospect of HTAQ in wearable electronic devices, aqueous flexible Zn//HTAQ batteries were assembled (Fig. S21 in Supporting information) and their electrochemical performance was investigated. The rate performance and The GCD curves for flexible Zn//HTAQ battery at different current densities are presented in Fig. 4a and Fig. S22 (Supporting information), respectively, showing that it can deliver the maximum discharge capacity of 366 mAh/g at 0.04 A/g. As the current density increases, average discharge capacity decreases, but, even at a high current density of 20 A/g, average discharge capacity remains at about 116 mAh/g, exhibiting a high-rate performance. When the current density returns to 0.04, 0.1, 0.5 and 1 A/g, the average discharge capacities can reach 184, 155, 130 and 122 mAh/g, respectively, showing a better reversibility. Fig. 4b displays the cycle stability of the flexible Zn//HTAQ battery at 2 A/g. As shown in Fig. 4b, the first discharge capacity is 121 mAh/g, the discharge capacity still delivers 81 mAh/g after 1900 cycles along with the capacity retention of 67 % and Coulombic efficiency of almost 100 %, revealing the flexible battery has also better cycle stability.

To look into the flexibility of the flexible Zn//HTAQ battery, its cycling stability at different folding angles was tested (Fig. 4c). After folding at a series of angles and cycling 5 times at each folding angle under the current density of 5 A/g, the battery can still get a capacity retention of 94 % when it turns back to the flat state, which indicates that there is no significant attenuation of capacity. The GCD curves at different folding angles displayed in Fig. 4d and Fig. S23 (Supporting information) show the discharge/charge capacities have no obvious change, indicating that folding does not significantly affect the stable operation of the flexible battery. The above facts reveal the flexible battery has good foldability and flexibility. The corresponding volumetric energy/power density of the flexible battery based on the data from Fig. S22 (Supporting information) is reflected in the Ragone diagram (Fig. 4e). The flexible Zn//HTAQ battery has a maximum volumetric energy density of 8.7 mWh/cm^3 and a maximum power density of 0.73 W/cm^3, higher than many previously reported flexible batteries and supercapacitors (Table S4 in Supporting information). In addition, it can be seen from Fig. 4f that two flexible Zn//HTAQ batteries could power a pattern (COF) consisting of 41 light-emitting diode (LED) lamps, demonstrating their great application potential in wearable electronics.

It is well known that the redox reaction that can effectively realize electron transfer is dominated by the difference (ΔE) in redox potential between the reactants [17]. Based on the CV curve of the Zn//HTAQ battery at 0.1 mV/s (Fig. S24 in Supporting information and Fig. 2b) and the Nernst equation, the calculated Zn^{2+}/H^+ extraction potential from the discharged HTAQ electrode (HTAQ-Zn-H) is −0.35, −0.21, −0.12 and 0.51 V (relative to the standard hydrogen electrode (SHE)), respectively. The potential values of −0.35, −0.21 and −0.12 V are larger than the standard electrode potential of oxygen (O_2) in the alkaline medium *vs.* SHE (0.40 V) [18]. Therefore, the ΔE between the discharged HTAQ electrode

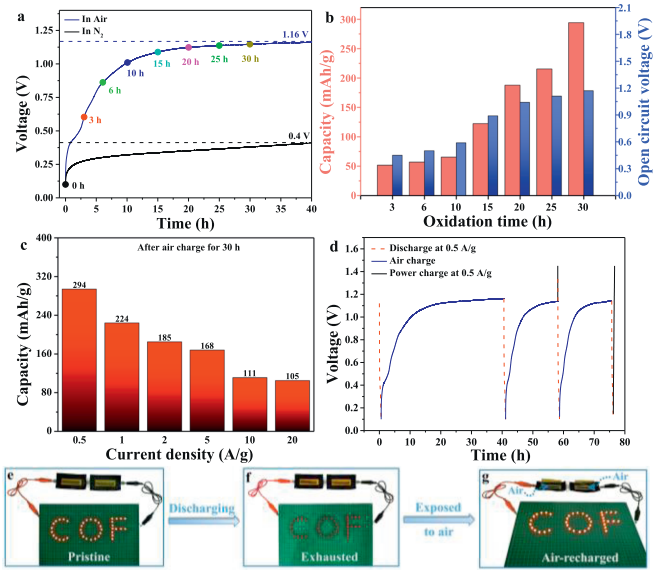


Fig. 5. Electrochemical properties of the discharged flexible Zn//HTAQ battery. (a) Charge curves in air and N_2 atmospheres. (b) Open circuit voltage (OCV) and discharge capacity at various oxidation times. (c) Discharge capacities at various rates after air-charge for 30 h. (d) Charging-discharging performance at galvanostatic charging or/and air-charging hybrid modes. (e-g) LED lights powered by two air-rechargeable Zn//HTAQ batteries at different states.

(HTAQ-Zn-H) and O_2 is greater than zero, indicating that the redox reaction between them is easy.

To demonstrate the feasibility of this reaction utilized to build air-charging (also called as chemically self-charging) AZBs, the chemical self-rechargeability of the flexible Zn//HTAQ batteries *via* air oxidation was investigated. Fig. 5a exhibits the results of the open circuit voltage (OCV) tests using the discharged flexible Zn//HTAQ batteries. In the OCV test, the discharged flexible Zn//HTAQ batteries were discharged to 0.1 V, which was followed with an OCV rest step at different gas atmospheres (*i.e.*, with exposure in air; with N_2 flow). As shown in Fig. 5a, when the discharged battery is exposed to air, the voltage gradually increases from 0.1 V to 1.2 V around after 40 h. However, in the absence of O_2 (*i.e.*, with N_2 flow), the voltage can only increase from 0.1 V to 0.4 V even after 40 h. Obviously, the above results show that the discharged flexible aqueous Zn//HTAQ battery can be chemically self-recharged *via* O_2 from air, meaning this battery has air-rechargeability. To determine the rate of the chemical self-charging, we collected the galvanostatic discharge curves of these discharged batteries after being oxidized at different times (Fig. 5b, Figs. S25a and b in Supporting information). With the increase in oxidation duration, the open circuit voltage (OCV) of the Zn//HTAQ battery continues to increase. As marked in Fig. 5b, after 15 h oxidation, the OCV of the discharged battery recovers to 0.89 V and the corresponding discharge capacity can reach 122 mAh/g at 0.5 A/g. When the oxidation time extends to 30 h, the OCV recovers to 1.2 V around and the discharge capacity further increases to 294 mAh/g, which is higher than that of many air-charging AZBs previously reported (Table S5 in Supporting information) [17–21]. Obviously, the discharge capacity of the flexible air-rechargeable battery is higher than that of the sealed flexible battery above mentioned, which might be related to the chemical oxidation induced by the dissolved O_2 in the aqueous electrolyte. We also investigated the rate capability of the chemical self-charging battery (Fig. 5c and Fig. S25c in Supporting information). After air-charging for 30 h, under current densities of 0.5, 1.0, 2.0, 5.0, 10, and 20 A/g, discharge capacities of the battery have 294, 224, 185, 168, 111, and 105 mAh/g, respectively, showing superior rate performance. Additionally, we have also observed that the discharge capacities of the flexible Zn//HTAQ battery after air-recharging surpass the galvanostatic discharge capacities at the current density range of 0.5–5 A/g. This phenomenon can be attributed to residual air within the battery upon resealing. In addition, as displayed in Fig. S25d, the Zn//HTAQ battery can carry out 15 repeated cycles of galvanostatic discharge and chemical self-charging, revealing it owns higher self-charging stability than many chemically self-charging zinc batteries reported [18,22,23,52,65–67]. As shown in Fig. 5d, the battery can be galvanostatic charged to 1.45 V when the external power supply is available. When the battery is self-charged in air, the OCV reaches over 1.13 V. Moreover, the galvanostatic discharging and self-charging modes can be seamlessly switched, and the battery can be recharged from a self-charged state (1.13 V) to a fully charged state (1.45 V) by an external power supply.

As shown in Figs. 5e-g, two flexible Zn//HTAQ batteries can be connected in series to light the LED lamps (COF). After the batteries were exhausted, the sealing Kapton film on the surface was removed to allow air to enter the batteries for charging (Fig. S26 in Supporting information). After chemically self-charging *via* air oxidation, two batteries connected in series can successfully drive the LED lights again for >2 h This result indicates that the air-rechargeable flexible Zn//HTAQ batteries could be available as chemically self-charging energy storage devices.

Furthermore, the redox process of the discharged HTAQ electrodes (HTAQ-nZn-(30–2n)H, simply named as HTAQ-Zn-H) in the process of air charging was systematically explored through various *ex-situ* characterization techniques, such as XPS, IR, and XRD. From XPS spectra in Figs. 6a and b, it can be seen that with the increase of air oxidation time, the peak intensity for C=N (399.8 eV) and C=O (533.2 eV) gradually increases, while the peak intensity of NH- (400.1 eV), C–N (400.8 eV), C–O (534.3 eV) and -OH (535.1 eV) gradually decreases, revealing the removal of H^+ ions from the discharged HTAQ electrode (HTAQ-Zn-H electrode) during air-charging. However, the intensity of N-Zn (399.3 eV) and O-Zn (531.5 eV) remains nearly unchanged, indicating that Zn^{2+} ions are almost not extracted from the HTAQ-Zn-H host. Such judgment was also proved by the XPS spectra of Zn 2p at the different air-charging time points for the HTAQ-Zn-H electrode (Fig. S27 in Supporting information). From Fig. S27, it can be found that the peak integral area of Zn $2p_{3/2}$ and Zn $2p_{1/2}$ is almost unchanged with the increase of air-charging time, indicating that Zn^{2+} is nearly not removed from the HTAQ-Zn-H electrode during the air-charging process. The production of this phenomenon should be ascribed to the standard electrode potential of oxygen (0.40 V *vs.* SHE) is lower than Zn^{2+}-extraction potential (0.51 V *vs.* SHE, Fig. S24). That is to say, almost only H^+ ions removal appears in the oxidation process of the HTAQ-Zn-H electrode by O_2. In the meantime, the removal of H^+ ions is confirmed by the IR spectra in Fig. 6c. As the oxidation reaction continues, the intensity of the characteristic peak (1629 cm^{-1}) that relates to the C=N/C=O bond stretching vibrations gradually increases, indicating that the HTAQ-Zn-H electrode can undergo spontaneous oxidation by oxygen in air. It can be observed in the XRD patterns that the diffraction peak at about $2\theta = 10.5°$, moves to a higher angle during the oxidation time from 0 to 30 h (Fig. 6d), corresponding to the decrease of interlayer spacing. This peak moving is ascribed to the extraction of H^+ ions from the HTAQ-Zn-H electrode. Based on the above results and discussion, the possible cathode reaction mechanism in the air-recharging process is proposed (Fig. S28 in Supporting information). In this process, the reaction between O_2 and H_2O produces OH^- ions *via* O_2 accepting electrons from HTAQ-Zn-H, then, the interaction of OH^- ions with extracted H^+ produces H_2O. Similar air-chargeable

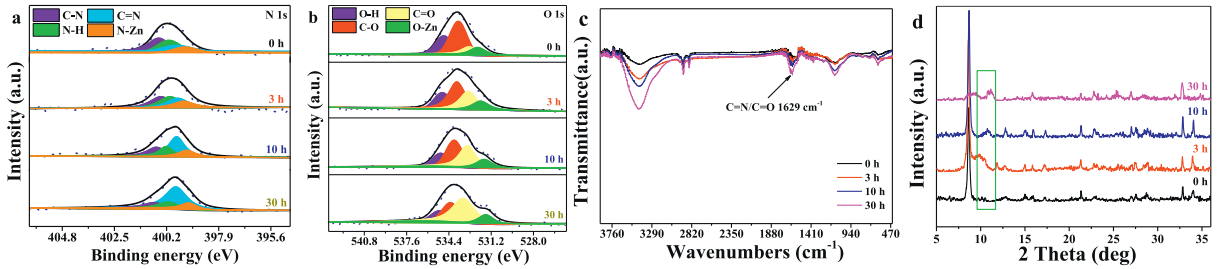


Fig. 6. Various *ex-situ* tests of the discharged HTAQ electrodes *via* different oxidation times. XPS spectra of (a) N 1s and (b) O 1s . (c) FT-IR spectra. (d) XRD patterns.

process has been observed in two organic small molecule-based cathodes reported recently [22,23].

In summary, we have successfully synthesized a porous organic polymer HTAQ and investigated it as a cathode material for AZBs. Due to its conjugated structure with multiple active sites (C=N and C=O groups) and insolubility in electrolytes, the assembled coin-type and flexible AZBs based on HTAQ cathode not only display better rate performance and excellent cycle life, but also superior energy density (104 Wh/kg) and remarkable volumetric energy density (8.7 mWh/cm^3), respectively. The storage energy mechanism of HTAQ involved in the co-insertion/co-removal of Zn^{2+} and H^+ ions was demonstrated by DFT calculation and the *ex-situ* physical and chemical measurements. Importantly, after the flexible Zn//HTAQ battery is exhausted, the battery can be chemically self-charged by being exposed to air atmosphere along with the removal of H^+. The AZBs with air-charging capability can avoid the limitations of battery recharging and reuse in harsh environment or remote areas, where the electrical grid is unavailable. After air-charging for 30 h, the exhausted (fully discharged) flexible Zn//HTAQ battery can be self-recharged to 1.2 V around without any external power supply, and exhibits a considerable discharge capacity of 294 mAh/g at 0.5 A/g, a high-rate performance (105 mAh/g at 20 A/g) and the higher chemically self-charging stability (15 cycles). More importantly, these air-rechargeable flexible Zn//HTAQ batteries are compatible with different chemical or/and galvanostatic charging hybrid modes. To our knowledge, this is the first report about chemically self-charging AZBs based on POPs cathodes *via* air. This work provides a new way to develop high-performance and flexible chemically self-charging AZBs.

Declaration of competing interest

The authors declare that they have no known competing financial interests or personal relationships that could have appeared to influence the work reported in this paper.

CRediT authorship contribution statement

Xiaojuan Chen: Writing – review & editing, Writing – original draft, Methodology, Investigation, Formal analysis, Data curation. **Yanwei Ma:** Writing – review & editing, Writing – original draft, Methodology, Investigation, Formal analysis, Data curation. **Yiwen Lu:** Validation. **Huimin Zhang:** Validation. **Baozhu Yang:** Software. **Qi Liu:** Writing – review & editing, Supervision, Resources, Project administration, Funding acquisition, Conceptualization.

Acknowledgments

This work was supported by the National Natural Science Foundation of China (No. 21975034) and the Postgraduate Research & Practice Innovation Program of Jiangsu Province (No. KYCX24_3170), the Project Funded by the Priority Academic Program Development of Jiangsu Higher Education Institutions. Thanks to the High Performance Computation Laboratory of Changzhou University and the Institute of Theoretical Chemistry of Jilin University.

Supplementary materials

Supplementary material associated with this article can be found, in the online version, at doi:10.1016/j.cclet.2024.110666.

References

[1] S. Chu, A. Majumdar, Nature 488 (2012) 294–303.
[2] L. Xue, Y. Li, H. Gao, et al., J. Am. Chem. Soc. 139 (2017) 2164–2167.
[3] N. Zhang, X. Chen, M. Yu, et al., Chem. Soc. Rev. 49 (2020) 4203–4219.
[4] B. Tang, L. Shan, S. Liang, J. Zhou, Energy Environ. Sci. 12 (2019) 3288–3304.
[5] P. Yu, Y. Zeng, H. Zhang, et al., Small 15 (2019) 1804760.
[6] Z. Wei, X. Wang, T. Zhu, et al., Chin. Chem. Lett. 35 (2024) 108421.
[7] J. Lu, T. Wang, J. Yang, et al., Angew. Chem. Int. Ed. 63 (2024) e202409838.
[8] B. Dunn, H. Kamath, J. Tarascon, Science 334 (2011) 928.
[9] X. Shi, W. Chen, T. Zhang, J. Zou, Z. Chen, Energy Environ. Sci. 14 (2021) 729–764.
[10] H. Khan, N. Mahmood, A. Zavabeti, et al., Nat. Commun. 11 (2020) 3449.
[11] Y. Luo, X. Cao, Z. Wang, Nano Energy 107 (2023) 108097.
[12] B. Boruah, A. Mathieson, B. Wen, et al., Nano Lett. 20 (2020) 5967–5974.
[13] B. Kim, M. Lee, V. Dilimon, et al., Energy Environ. Sci. 13 (2020) 1473.
[14] L. Jin, X. Xiao, W. Deng, et al., Nano Lett. 20 (2020) 6404–6411.
[15] Y. Liu, W. Liu, Z. Wang, et al., Nat. Commun. 11 (2020) 1599.
[16] L. Ma, Y. Zhao, X. Ji, et al., Adv. Energy Mater. 9 (2019) 1900509.
[17] C. Liu, W. Xu, C. Mei, et al., Adv. Energy Mater. 11 (2021) 2003902.
[18] Y. Zhang, F. Wan, S. Huang, et al., Nat. Commun. 11 (2020) 2199.
[19] L. Yan, Y. Zhang, Z. Ni, et al., J. Am. Chem. Soc. 143 (2021) 15369–15377.
[20] M. Liao, J. Wang, L. Ye, et al., J. Mater. Chem. A 9 (2021) 6811–6818.
[21] W. Qiu, Z. Lin, H. Xiao, et al., Mater. Adv. 2 (2021) 6694–6702.
[22] Z. Tie, Y. Zhang, J. Zhu, S. Bi, Z. Niu, J. Am. Chem. Soc. 144 (2022) 10301–10308.
[23] X. Chen, H. Su, B. Yang, et al., Chin. Chem. Lett. 35 (2024) 108487.
[24] J. Shi, K. Mao, Q. Zhang, et al., Nano-Micro Lett. 15 (2023) 53.
[25] M. Zhang, T. Hu, X. Wang, et al., Energy Storage Mater. 51 (2022) 465–475.
[26] S. Zhang, G. Cheng, L. Guo, et al., Angew. Chem. Int. Ed. 59 (2020) 6007–6014.
[27] L. Zhang, R. Wang, Z. Liu, et al., Adv. Mater. 35 (2023) 2210082.
[28] J. Wang, Z. Liu, H. Wang, F. Cui, G. Zhu, Chem. Eng. J. 450 (2022) 138051.
[29] Q. Gu, J. Zha, C. Chen, et al., Adv. Mater. 36 (2024) 2306414.
[30] C. Wu, M. Hu, X. Yan, et al., Energy Storage Mater. 36 (2021) 347–354.
[31] J. Park, M. Kwak, C. Hwang, et al., Adv. Mater. 33 (2021) 2101726.
[32] S. Zheng, L. Miao, T. Sun, et al., J. Mater. Chem. A. 9 (2021) 2700–2705.
[33] R. Shi, L. Liu, Y. Lu, et al., Nat. Commun. 11 (2020) 178.
[34] A. Schneemann, R. Dong, F. Schwotzer, et al., Chem. Sci. 12 (2021) 1600–1619.
[35] J. Sun, Y. Fei, H. Tang, et al., ACS Appl. Energy Mater. 7 (2024) 7592–7602.
[36] Y. Zhao, C. Yang, Y. Yu, Chin. Chem. Lett. 35 (2024) 108865.
[37] C. Ding, Y. Wang, C. Li, et al., Chem. Sci. 15 (2024) 4952–4959.
[38] K. Nam, H. Kim, Y. Beldjoudi, et al., J. Am. Chem. Soc. 142 (2020) 2541–2548.
[39] M. Na, Y. Oh, H. Byon, Chem. Mater. 32 (2020) 6990–6997.
[40] Y. Gao, G. Li, F. Wang, et al., Energy Storage Mater. 40 (2021) 31–40.
[41] Y. Zhang, Y. Liang, H. Dong, X. Wang, Y. Yao, J. Electrochem. Soc. 167 (2020) 070558.
[42] Y. Wang, C. Wang, Z. Ni, et al., Adv. Mater. 32 (2020) 2000338.
[43] J. Xie, F. Yu, J. Zhao, et al., Energy Storage Mater. 33 (2020) 283–289.
[44] D. Kundu, P. Oberholzer, C. Glaros, A. Bouzid, E. Tervoort, Chem. Mater. 30 (2018) 3874–3881.
[45] Q. Zhao, W. Huang, Z. Luo, et al., Sci. Adv. 4 (2018) eaao1761.
[46] Z. Guo, Y. Ma, X. Dong, et al., Angew. Chem. Int. Ed. 57 (2018) 11737–11741.
[47] W. Wang, V. Kale, Z. Cao, et al., ACS Energy Lett. 5 (2020) 2256–2264.
[48] G. Sun, B. Yang, X. Chen, et al., Chem. Eng. J. 431 (2022) 134253.
[49] Z. Ye, S. Xie, Z. Cao, et al., Energy Storage Mater. 37 (2021) 378–386.
[50] X. Chen, H. Su, B. Yang, G. Yin, Q. Liu, Sustain. Energy Fuel 6 (2022) 2523–2531.
[51] Z. Tie, L. Liu, S. Deng, D. Zhao, Z. Niu, Angew. Chem. Int. Ed. 59 (2020) 4920–4924.

[52] Y. Lu, L. Su, B. Yang, et al., Chem. Eng. J. 484 (2024) 149531.
[53] W. Wang, V. Kale, Z. Cao, et al., Adv. Mater. 33 (2021) 2103617.
[54] H. Zhang, X. Liu, X. Chen, et al., J. Energy Storage 78 (2024) 110326.
[55] T. Brezesinski, J. Wang, S. Tolbert, B. Dunn, Nat. Mater. 9 (2010) 146–151.
[56] J. Wang, J. Polleux, J. Lim, B. Dunn, J. Phys. Chem. C 111 (2007) 14925–14931.
[57] F. Wan, L. Zhang, X. Dai, et al., Nat. Commun. 9 (2018) 1656.
[58] H. Shi, Y. Ye, K. Liu, Y. Song, X. Sun, Angew. Chem. Int. Ed. 57 (2018) 16359–16363.
[59] X. Dai, F. Wan, L. Zhang, H. Cao, Z. Niu, Energy Storage Mater. 17 (2019) 143–150.
[60] W. Li, K. Wang, S. Cheng, K. Jiang, Energy Storage Mater. 15 (2018) 14–21.
[61] Z. Li, Y. Zhang, J. Xu, Y. Wang, Batteries Supercaps 6 (2023) e202200431.
[62] N. Wang, X. Dong, B. Wang, et al., Angew. Chem. Int. Ed. 59 (2020) 14577–14583.
[63] H. Zhang, Y. Fang, F. Yang, X. Liu, X. Lu, Energy Environ. Sci. 13 (2020) 2515–2523.
[64] L. Zhang, L. Chen, X. Zhou, Z. Liu, Adv. Energy Mater. 5 (2015) 1400930.
[65] X. Liu, G. Sun, H. Zhang, et al., J. Energy Storage 96 (2024) 112736.
[66] X. Song, H. Su, X. Chen, et al., ACS Sustain. Chem. Eng. 12 (2024) 3153–3166.
[67] W. Su, Y. Zhang, H. Wang, M. Yang, Z. Niu, Adv. Mater. 36 (2023) 2308042.